

# Bio-Heat Model of Kilohertz-Frequency Deep Brain Stimulation Increases Brain Tissue Temperature

Niranjan Khadka, PhD Candidate\* ; Irene E. Harmsen, MD/PhD Candidate<sup>†</sup>; Andres M. Lozano, MD, PhD<sup>†</sup>; Marom Bikson, PhD\*

**Objectives:** Early clinical trials suggest that deep brain stimulation at kilohertz frequencies (10 kHz-DBS) may be effective in improving motor symptoms in patients with movement disorders. The 10 kHz-DBS can deliver significantly more power in tissue compared to conventional frequency DBS, reflecting increased pulse compression (duty cycle). We hypothesize that 10 kHz-DBS modulates neuronal function through moderate local tissue heating, analogous to kilohertz spinal cord stimulation (10 kHz-SCS). To establish the role of tissue heating in 10 kHz-DBS (30  $\mu$ s, 10 kHz, at intensities of 3-7 mA<sub>peak</sub>), a decisive first step is to characterize the range of temperature changes during clinical kHz-DBS protocols.

**Materials and Methods:** We developed a high-resolution magnetic resonance imaging-derived DBS model incorporating joule-heat coupled bio-heat multi-physics to establish the role of tissue heating. Volume of tissue activated (VTA) under assumptions of activating function (for 130 Hz) or heating (for 10 kHz) based neuromodulation are contrasted.

**Results:** DBS waveform power (waveform RMS) determined joule heating at the deep brain tissues. Peak heating was supra-linearly dependent on stimulation RMS. The 10 kHz-DBS stimulation with 2.3 to 5.4 mA<sub>RMS</sub> (corresponding to 3 to 7 mA<sub>peak</sub>) produced 0.10 to 1.38°C heating at the subthalamic nucleus (STN) target under standard tissue parameters. Maximum temperature increases were predicted inside the electrode encapsulation layer (enCAP) with 2.3 to 5.4 mA<sub>RMS</sub> producing 0.13 to 1.87°C under standard tissue parameters. Tissue parameter analysis predicted STN heating was especially sensitive (ranging from 0.44 to 1.35°C at 3.8 mA<sub>RMS</sub>) to decreasing enCAP electrical conductivity and decreasing STN thermal conductivity.

**Conclusions:** Subject to validation with *in vivo* measurements, neuromodulation through a heating mechanism of action by 10 kHz-DBS can indicate novel therapeutic pathways and strategies for dose optimization.

**Keywords:** Bio-heat, computational modeling, deep brain stimulation, kilohertz-frequency, Senza HF10, temperature

**Conflict of Interest:** The City University of New York (CUNY) has IP on neuro-stimulation systems and methods with authors Niranjan Khadka and Marom Bikson as inventors. Marom Bikson has equity in Soterix Medical. Marom Bikson serves on the advisory boards of Boston Scientific, Mectra, and GlaxoSmithKline Inc. Andres M. Lozano serves as a consultant for Nevro. Irene E. Harmsen has no conflicts of interest to disclose.

## INTRODUCTION

In the first study examining deep brain stimulation (DBS) at 10 kHz frequencies (10 kHz-DBS; also called ultra-high frequency DBS), we reported that acute 10 kHz-DBS appears safe and may be effective in improving motor symptoms in patients with movement disorders (1). Furthermore, 10 kHz-DBS stimulation may have the potential to reduce stimulation-induced adverse effects, such as transient paresthesia and impaired speech, which are often encountered with DBS at conventional frequencies (2–4). Selecting the optimal stimulation frequency for DBS can be challenging. Perceived loss of DBS efficacy at low kHz (<5 kHz) derives from historical findings in limited parameter space (e.g., voltage-controlled, specific duty cycle) (5), which was supported by models of conventional mechanisms of action (6). Another factor that encourages the use of lower DBS frequencies is battery life (7); we note that increased power consumption is delivered into the electrode and subsequently into the surrounding deep brain tissue (8).

Marom Bikson, PhD, Department of Biomedical Engineering, The City College of New York, 85 Saint Nicholas Terrace, New York, NY 10031, USA.

Email: bikson@ccny.cuny.edu,

Niranjan Khadka, PhD Candidate Department of Biomedical Engineering, The City College of New York, 85 Saint Nicholas Terrace, New York, NY 10031, USA.

Email: nkhadka@ccny.cuny.edu

\* Department of Biomedical Engineering, The City College of New York, New York, NY, USA; and

<sup>†</sup> Division of Neurosurgery, Department of Surgery, Toronto Western Hospital, University of Toronto, Toronto, ON, Canada

Source(s) of Financial Support: This study was partially funded by grants from NIH (NIH-NIMH 1R01MH111896, NIH-NINDS 1R01NS101362, NIH-NCI U54CA137788/ U54CA132378, R03 NS054783) New York State Department of Health (NYS DOH, DOH01-C31291GG), and cycle 50 PSC-CUNY.

For more information on author guidelines, an explanation of our peer review process, and conflict of interest informed consent policies, please go to <http://www.wiley.com/WileyCDA/Section/id-301854.html>

The emergence of spinal cord stimulation (SCS) at 10 kHz (9–13) has encouraged the exploration of novel neuromodulation mechanisms, including our hypothesis of tissue warming, based on the relatively high-power nature of clinical 10 kHz waveforms (14). Since heating of deep brain tissue will impact a myriad of neuronal functions linked to clinical efficacy (see Discussion), a pivotal step to establish the role of moderate local heating in 10 kHz-DBS is predicting the degree of temperature increases. To this end, we expanded on our earlier phantom-verified bio-heat model of conventional rate DBS (15,16), incorporating detailed MRI-derived representation of inhomogeneous local tissues, and emulating clinical 10 kHz-DBS protocols.

## METHODS

### Bio-Heat DBS Model Construction and Solution Method

High-resolution magnetic resonance imaging (MRI) scans of standard human head (unsampled to 0.18 mm) were segmented (Simpleware, Synopsys Inc., CA, USA) into the following tissue masks: skin; skull; CSF; air; gray-matter; white-matter; cingulate gyrus; basal ganglia; corpus callosum; thalamus; subthalamic nucleus (STN); fornix; nucleus accumbens; hippocampus; amygdala; midbrain; mammillary bodies; pons; medulla oblongata; and insula. Computer-aided design (CAD) model of a clinical DBS lead (Medtronic 3387; 4 contacts (0, 1, 2, and 3) Pt/Ir DBS lead, contact length: 1.5 mm, inter-contact distance: 1.5 mm, diameter: 1.27 mm) was modeled in SolidWorks (Dassault Systemes Corp., MA, USA) and imported into the head model. A 0.5 mm thick encapsulation layer around the DBS lead with standard assigned conductivity (0.13 S/m) matched the clinical impedance values (~1 k $\Omega$ ) (17). The lead penetrated from the top of the skull at ~20 mm from the midline to the STN target at ~12 mm from the midline. Approximately, 7 mm of the STN was contacted around the lead: contact 0 (deepest contact) was at the ventral border of the STN, contacts 1 and 2 were inside the STN, and contact 3 was at the dorsal border of the STN (Fig. 1). The volumetric conductor model was then meshed using a voxel-based meshing algorithm, and an adaptive tetrahedral mesh of the head was generated following multiple mesh densities refinements (within in 1% error in voltage and current density at the STN).

The stimulation (Laplace equation for electrostatics [ $\nabla \cdot (\sigma \nabla V) = 0$  where  $V$  is potential and  $\sigma$  is conductivity]) coupled Pennes' bio-heat transfer equation (Eqn. (1)) including joule heating, metabolic heat generation rate ( $Q_{met}$ ), and blood perfusion rate ( $\omega_b$ ) in the brain tissues was solved.

$$\rho_p C_p \nabla T = \nabla \cdot (\kappa \nabla T) - \rho_b C_b \omega_b (T - T_b) + Q_{met} + \sigma |\nabla V|^2 \quad (1)$$

where  $\rho$ ,  $C_p$ ,  $T$ ,  $\sigma$ , and  $\kappa$  represent tissue density, specific heat, temperature, electrical conductivity, and thermal conductivity respectively.

Blood density ( $\rho_b$ ), specific heat ( $C_b$ ), and temperature ( $T_b$ ) were assumed constant in all vascularized brain tissues with corresponding values as 1045 kg/m<sup>3</sup>, 3600 J/(kg. K), and 36.7°C, respectively. Tissue specific perfusion rate ( $\omega_b$ ) ranged from 0.00063 to 0.0228 s<sup>-1</sup> (18,19). Prior to the application of 10 kHz-DBS, the  $Q_{met}$  required to balance the initial brain temperature was calculated using Eqn. (2) (20,21):

$$Q_{met} = \rho_b C_b \omega_b (T - T_b) \quad (2)$$

where  $T_b$  and  $T$  are initial blood and brain temperature.

The calculated  $Q_{met}$  values from Eqn. (2) for the corresponding  $\omega_b$  values of the brain tissues were: gray matter ( $\omega_b$ , 0.018 s<sup>-1</sup>;  $Q_{met}$ , 15540 Wm<sup>-3</sup>); white matter, corpus callosum, fornix, mammillary bodies ( $\omega_b$ , 0.008 s<sup>-1</sup>;  $Q_{met}$ , 4320 Wm<sup>-3</sup>); hippocampus ( $\omega_b$ , 0.00063 s<sup>-1</sup>;  $Q_{met}$ , 15540 Wm<sup>-3</sup>); midbrain ( $\omega_b$ , 0.028 s<sup>-1</sup>;  $Q_{met}$ , 11370 Wm<sup>-3</sup>); basal ganglia, thalamus, amygdala, cingulate, nucleus accumbens ( $\omega_b$ , 0.02282 s<sup>-1</sup>;  $Q_{met}$ , 15540 Wm<sup>-3</sup>); and STN ( $\omega_b$ , 0.02038 s<sup>-1</sup>;  $Q_{met}$ , 13930 Wm<sup>-3</sup>). Since CSF is avascular and enCAP is predominantly scar tissues, 0 values were assigned for  $Q_{met}$  and  $\omega_b$  were assigned. The balanced  $Q_{met}$  values approximated prior experimental measurements (18,19,22).

Thermo-electric properties ( $\sigma$ ,  $\kappa$ ) of the biological tissues were based on the following aggregate literature values (23,24): CSF (1.65 S/m, 0.57 W/[m.K]); gray matter, STN, thalamus, amygdala, basal ganglia, nucleus accumbens, and cingulate gyrus (0.276 S/m, 0.55 W/[m.K]); midbrain (0.126 S/m, 0.51 W/[m.K]); white matter, mammillary bodies, and fornix (0.126 S/m, 0.48 W/[m.K]); hippocampus (0.126 S/m, 0.55 W/[m.K]); corpus callosum (0.060 S/m, 0.48 W/[m.K]); and enCAP (0.13 S/m, 0.47 W/[m.K]). Electrical and thermal conductivities of the DBS contacts and insulating bands between contacts were (4E6 S/m, 31 W/[m.K]) and (0.0002 S/m, 0.026 W/[m.K]), respectively (25). In some simulations, the "standard" tissue conductivity parameters of enCAP and STN were manipulated by either doubling or halving.

Static RMS values were applied (Eqn. (3)) for tested clinical kHz-DBS intensities (3–7 mA<sub>peak</sub> at 30  $\mu$ s and 10 kHz), and this approach was supported by prior phantom verification for conventional DBS (16) and kHz-SCS (26,27).

$$I_{RMS} = I_{Peak} \sqrt{t * f} = I_{Peak} \sqrt{D} \quad (3)$$

where  $I_{RMS}$  is the corresponding RMS value of peak stimulation intensity ( $I_{Peak}$ ),  $t$  is the combined (anodic and cathodic phase) pulse width,  $f$  is the frequency, and  $D$  is the duty cycle.

Unless otherwise stated, contact 2 (C2) was energized in a monopolar electrode configuration as tested clinically (1). An inward normal current density ( $J_{norm, RMS}$ ) was applied to the electrode with the bottom surface of the model grounded. For bipolar electrode configuration, contact 2 (C2) was energized (anode), while contact 1 (C1) was grounded (cathode). Remaining outer boundaries of the head were electrically insulated. The temperature of the outer boundaries of the model was set to core body temperature (37°C) with no convection across outer head boundaries (28). The bio-heat 10 kHz-DBS model was then solved under the steady-state assumption and the corresponding temperature increases and field intensities were predicted. Temperature difference ( $\Delta T$ ) was calculated by subtracting tissue temperature increase by stimulation (joule heat) from tissue temperature increase without stimulation.

### Volume of Tissue Activated and Volume of Tissue Heated

An activating function-based approach (second derivative of the electric potential) was implemented to estimate the volume of tissue activation (VTA) for conventional rate (130 Hz) DBS (25,29–31). Specifically, the divergence of the gradient of the electric potential ( $\nabla^2 V_e$ ) (generalization of the second derivative of the electric potential in 3D) was used to approximate the VTA (25,31–34). Activation threshold levels for different axon diameters (0.36 V/mm<sup>2</sup> corresponding to 2.5  $\mu$ m or 0.82 V/mm<sup>2</sup> corresponding to 5  $\mu$ m) at conventional rate DBS were implemented to define the VTA (32). For volume of tissue heated (VTH) at 10 kHz-DBS, a  $\Delta T$  threshold of 0.1°C or 0.5°C was

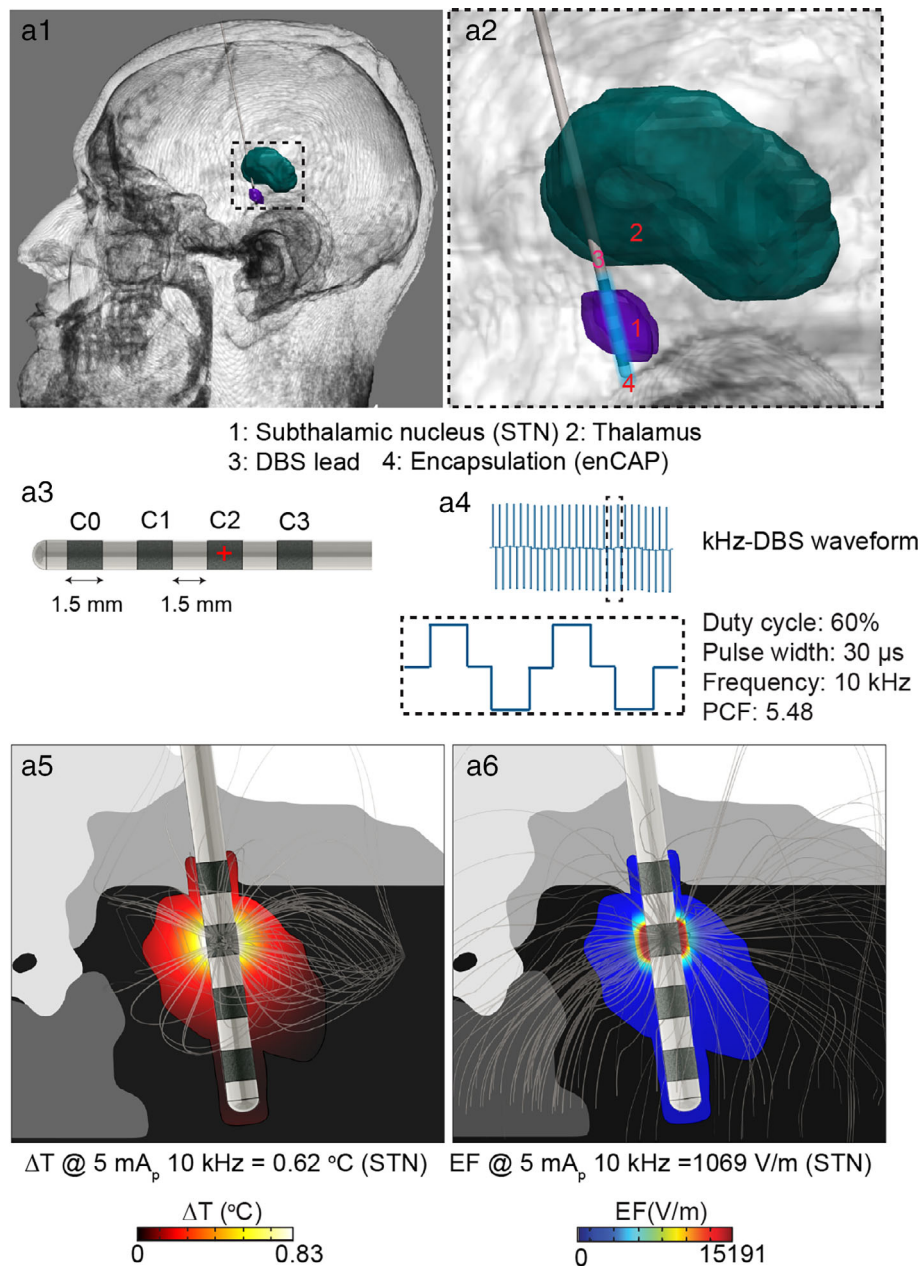


**Figure 1** FEM bio-heat model predicts temperature increases during kHz-DBS. (A1) A high-resolution human head model with segmented brain tissues and a DBS lead. For the illustration purpose, only STN (purple) and thalamus (green) are shown. (A2) Inset details model anatomy, showing the STN (1), thalamus (2), DBS lead (3) at the STN target, and an encapsulation layer (4). (A3) Clinical DBS lead (Medtronic DBS 3387) with contact C2 energized in a monopolar electrode configuration. (A4) Clinical DBS waveform at 10 kHz with 30  $\mu$ s pulse width per phase, resulting in a 5.48 Pulse Compression Factor (PCF) with 60% duty (see Ref (14) for details). Predicted temperature increases with heat flux streamlines (A5) and electric field distribution with current streamlines (A6) across deep brain tissues at 5  $\text{mA}_{\text{peak}}$  (3.8  $\text{mA}_{\text{RMS}}$ ). [Color figure can be viewed at [wileyonlinelibrary.com](http://wileyonlinelibrary.com)]

considered. Both VTA and VTH were determined at 3, 5, and 7 mA peak with monopolar and bipolar stimulation (Fig. 3).

## RESULTS

We developed an MRI-derived finite element method (FEM) bio-heat computational model of 10 kHz-DBS, with tissue specific electrical and thermal (passive and blood flow) properties (Fig. 1). For each simulation, RMS current intensities that corresponded to clinically tested peak current intensities were applied to the model.

Predicted peak temperature ( $\Delta T$ ) in the encapsulation layer (enCAP) and STN increased supralinearly as a function of stimulation intensity (standard tissue parameters, Fig. 2), reasonably fit by a power law (14). Under standard tissue parameters, monopolar kHz-DBS at 2.3  $\text{mA}_{\text{RMS}}$  (3  $\text{mA}_{\text{peak}}$ ) produces 0.13 $^\circ\text{C}$  temperature rise in the enCAP and 0.10 $^\circ\text{C}$  at the STN. At 3.8  $\text{mA}_{\text{RMS}}$  (5  $\text{mA}_{\text{peak}}$ ), temperature increases by 0.83 $^\circ\text{C}$  in the enCAP and 0.62 $^\circ\text{C}$  at the STN. Finally, at 5.4  $\text{mA}_{\text{RMS}}$  (7  $\text{mA}_p$ ), the temperature increases by 1.87 $^\circ\text{C}$  in the enCAP and 1.38 $^\circ\text{C}$  at the STN.

For 10 kHz monopolar DBS with 3.8  $\text{mA}_{\text{RMS}}$  (5  $\text{mA}_p$ ) intensity, we considered the sensitivity of heating to model tissue

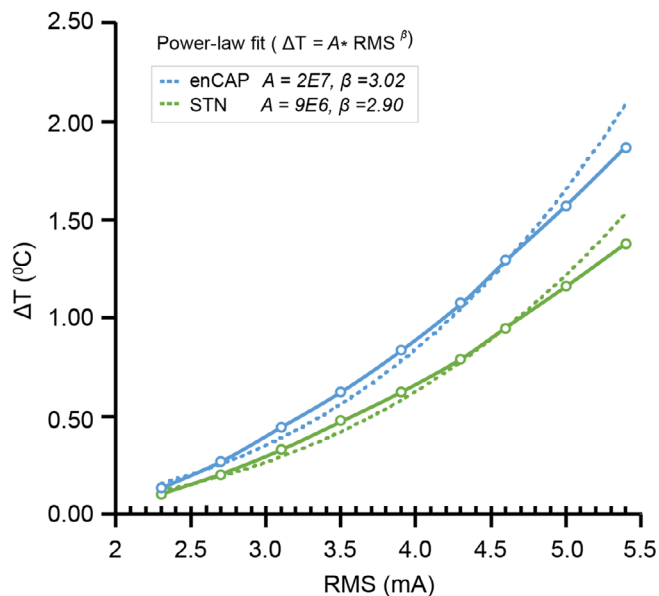


**Figure 2** Stimulation intensity (RMS) vs. temperature increases at encapsulation (enCAP) and STN. An MRI-derived FEM model of kHz-DBS predicts  $\Delta T$  increases supralinearly ( $\beta > 1$ ) with kHz-DBS RMS intensities (14). Results were fit according to a power law. [Color figure can be viewed at wileyonlinelibrary.com]

parameters, specifically doubling or halving the electrical and/or thermal conductivities of either the STN or enCAP (Table 1). Decreasing the electrical or thermal conductivity of either STN or enCAP always increased heating of both STN and enCAP. Heating of both the STN and enCAP was the most sensitive to reducing enCAP electrical conductivity (enCAP;  $\sigma/2, \kappa$ ), namely heating the 10 kHz-DBS increased the most with reducing enCAP conductivity compared to any other tissue parameter tested. STN heating was next more sensitive to reducing STN thermal conductivity (STN;  $\sigma, \kappa/2$ ) while enCAP heating was next more sensitivity to reducing enCAP thermal conductivity (enCAP  $\sigma, \kappa/2$ ). Maximum temperature rises in both STN (1.35°C) and enCAP (2.53°C) were predicted for enCAP  $\sigma/2, \kappa/2$ . Minimal temperature rises in both STN (0.02°C) and enCAP (0.10°C) were predicted for STN  $2\sigma, 2\kappa$ . In any combination tested, the  $\Delta T$  was always higher in enCAP compared to the STN, except the ( $2\sigma, 2\kappa$ ) condition where heating in the STN was slightly greater than enCAP.

Activation thresholds corresponding to either 2.5  $\mu\text{m}$  or 5  $\mu\text{m}$  axon diameter stimulation at conventional rate DBS (130 Hz) defined the VTA. VTH thresholds of  $\Delta T$  0.1°C and 0.5°C were applied for 10 kHz-DBS. As a first approximation, under the assumptions simulated here, the volumes of VTA and VTH are comparable for the same dose. This may suggest that stimulation and heating have some additive effect in neural activation (neuromodulation). For a given current intensity and VTA/VTH threshold, both VTA and VTH roughly doubled for bipolar vs. monopolar montages. Both VTA and VTH increased supralinearly with stimulation intensities (3, 5, and 7 mA peak) and both bipolar and monopolar electrode configurations. For 7 mA (peak) bipolar and monopolar electrode configuration, the VTA and VTH spread beyond the STN. With monopolar 130 Hz DBS, the VTA were 14.15, 31.63, and 54.54  $\text{mm}^3$  at 0.36  $\text{V}/\text{mm}^2$  activation threshold, and 2.15, 5.83, and 10.81  $\text{mm}^3$  at 0.82  $\text{V}/\text{mm}^2$  activation threshold, for 3, 5, and 7 mA, respectively. The VTA for bipolar 130 Hz DBS at 3, 5, and 7 mA peak intensities were 28.51, 58.21, and 90.94  $\text{mm}^3$  at 0.36  $\text{V}/\text{mm}^2$  threshold, and 4.53, 12.33, 22.28  $\text{mm}^3$  at 0.82  $\text{V}/\text{mm}^2$  threshold. When thresholding at 0.1°C, the VTH for monopolar 10 kHz DBS were 2.61, 39.29, and 135.19  $\text{mm}^3$  and at a threshold 0.5°C, the VTH were 0, 5.34, 23.55  $\text{mm}^3$  for 3, 5, and 7 mA peak, respectively. For a bipolar 10 kHz DBS, the VTH were 9.69, 135.66, and 298.23  $\text{mm}^3$  at 0.1°C threshold, and 0, 20.62, and 82.99  $\text{mm}^3$  at 0.5°C threshold for 3, 5, and 7 mA peak, respectively (Fig. 3).

## DISCUSSION

Our initial clinical findings on kHz-DBS are of interest because they open up a new therapeutic stimulation parameter space for future study and development (1). A heating mechanism of action (MoA) augments such considerations. For example, since heating depends only (and supralinearly) on waveform RMS independent of other parameters, optimal electrode placement and lead resistance may differ following heating vs. conventional MoA.

The biophysics of heating are analogous experimentally verified prior simulations of conventional rate DBS (15,16) and kHz SCS (14,26,27), however comparisons highlight the importance of stimulation dose (electrodes and waveform) as well as tissue anatomy and parameters. Compared to monopolar stimulation, energizing an adjacent contact in a bipolar electrode configuration may further increase temperature (15). This is compounded by

**Table 1.** Conductivity Sensitivities Analysis at 3.8  $\text{mA}_{\text{RMS}}$  (5  $\text{mA}_p$ ) of the enCAP and STN.

enCAP conductivity sensitivities			STN conductivity sensitivities			
Conductivities	$\Delta T$ (°C)		Resistance ( $\Omega$ )	$\Delta T$ (°C)		Resistance ( $\Omega$ )
	enCAP	STN		enCAP	STN	
( $\sigma, \kappa$ )	0.83	0.62	747	0.83	0.62	747
( $\sigma, \kappa/2$ )	1.22	0.66	747	1.18	1.00	747
( $\sigma, 2\kappa$ )	0.60	0.55	747	0.61	0.36	747
( $2\sigma, \kappa$ )	0.36	0.28	520	0.77	0.55	660
( $2\sigma, \kappa/2$ )	0.56	0.30	520	1.09	0.91	660
( $2\sigma, 2\kappa$ )	0.23	0.24	520	0.10	0.02	660
( $\sigma/2, \kappa$ )	1.77	1.27	1175	0.95	0.72	885
( $\sigma/2, \kappa/2$ )	2.53	1.35	1175	1.34	1.15	885
( $\sigma/2, 2\kappa$ )	1.31	1.14	1175	0.70	0.44	885

Properties of the enCAP (left) or STN (right) were changed independently with resulting heating ( $\Delta T$ ) of both enCAP and STN reported. Tissue electrical conductivity ( $\sigma$ ) and/or thermal conductivity ( $\kappa$ ) were doubled or halved. Total lead resistance ( $\Omega$ ) for each condition is also reported.

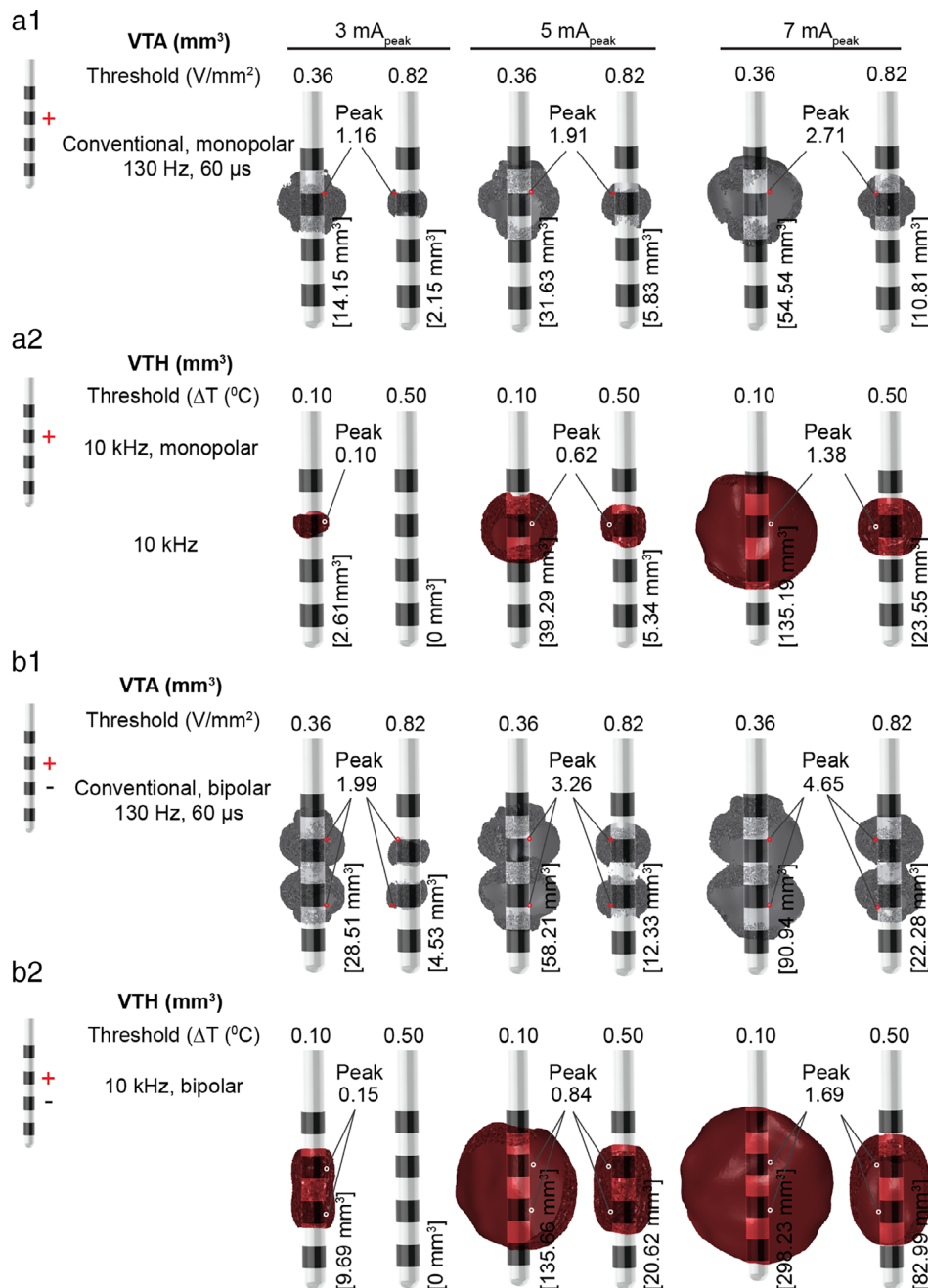


**Figure 3** Activating function-based VTA at conventional rate DBS (130 Hz at 60 μs), and VTH at 10 kHz-DBS with monopolar or bipolar electrode configuration at 3, 5, and 7 mA peak with different thresholds. VTA and VTH both increase supralinearly with stimulation intensities and expand twice with bipolar montage vs. monopolar montages. [Color figure can be viewed at [wileyonlinelibrary.com](http://wileyonlinelibrary.com)]

reduced inter-electrode distances (e.g., Medtronic 3389 vs. 3387 lead designs) (15). In kHz-SCS, the highly resistive epidural space plays a central role in temperature increases both at the lead and at the spinal cord (14). Here, the encapsulation layer plays a similar role in kHz-DBS (Table 1), despite the difference in anatomy in both kHz-SCS and kHz-DBS cases, a high resistive tissue at the electrode surface increases joule heat deposition, which is then conducted to more distant tissue (35).

Notably, while increasing tissue resistivity increases heating for current-controlled stimulation, increasing tissue resistivity decreases heating for voltage-controlled stimulation (15). As such, the enCAP may increase heating under current controlled

while decreases heating under voltage controlled stimulation. All these device and tissue parameters interact; for example, voltage-controlled DBS at conventional rates with low impedance (minimal encapsulation layer) may also produce significant heating (15,16). However, by virtue of a higher pulse compression factor (PCF (14)), kHz-DBS can achieve higher temperature. The FDA guidelines for MRI-safety allow less than 2°C over 1 hour of exposure at 1.5 T and 3.0 T frequencies (36) with MRI compatible system resulting in 0.3 to 3.6°C (37,38). Functional tissue ablation specifically using DBS leads involves RMS intensities of 19 mA or more, produced a peak heating of ~69.52°C per our quadratic standard model. Generally, RF-ablation of deep brain

aims for 42 to 49°C, although interestingly a transient temperature increases to 45°C can produce reversible functional lesions (39). Animal studies indicate reversible functional lesioning, for short exposures, at temperatures >46°C (40).

The precise degree of heating during kHz-DBS will depend on lead design, electrode selection, waveform (stimulation RMS), and passive and active tissue properties (Table 1 and Fig. 3). Nevertheless, the DBS bioheat models developed here support predicting and optimizing heating across DBS approaches. This can be informed and contrasted to models of conventional-rate (e.g. 130 Hz) DBS. In general, for both VTA and VTH, one can consider the brain area of modulation (perimeter of volume maps) and the nature of neuromodulation within the volume (threshold used for given volume map). For VTA, this analysis addresses fiber activation of various types (predicted by activating function threshold), whereas for VTH, this analysis will depend on yet-unspecified neurophysiological process (predicted by temperature threshold). Both VTA and VTH increase supralinearly with stimulation intensities (Fig. 3 (41)) and expand ~2x with bipolar vs. monopolar montages (Fig. 3 (42,43)). Increasing the tissue resistivities (e.g., enCAP or STN resistivities) increase both VTA and VTH under current-controlled stimulation, while decreasing both VTA and VTH under voltage-controlled stimulation (data not shown (44)). Depending on dose, either VTH or VTA may expand beyond the (targeted) STN, with implications for efficacy or the therapeutic window (Fig. 3 (45–48)).

While the specific mechanisms of heating-based neuromodulation (at different VTH temperature thresholds) remain to be shown, the principle of heating-based neuromodulation is established. All brain tissues are sensitive to temperature variations. Neuronal excitability, neurotransmitter function and plasticity, underlying metabolic functions, and connectivity and synchronization are all modulated by heating (49–53). Indeed, there is a long-standing record of neuromodulation techniques that are associated with heating and reversible changes in brain excitability including transcranial focused ultrasound (54) and infrared stimulation (55). A heating MoA of DBS suggests multiple plausible therapeutic pathways. Validating temperature increases with *in vivo* measures and characterizing such novel therapeutic cascades would suggest new avenues for DBS neuromodulation. Optimization approaches may approximate or differ from those based on conventional mechanisms (VTA vs. VTH) (31,56,57), including the role of impedance in voltage vs. current control (58), impact of smaller electrodes as used in directional leads (59–62), and waveforms not dependent on pulse characteristics (63). Computational models are both subject to experimental verification and underpin animal and human trials on the mechanism of action (4,64–69), such that the novel theoretical framework developed here informs new avenues of DBS research and optimization. Tissue heating during kHz-DBS would interact with any coincident theoretical mechanisms of action (e.g., electro-permeation of the blood brain barrier (70), conduction block (6), etc.).

## Authorship Statement

Niranjan Khadka and Marom Bikson designed and prepared the manuscript with novel inputs. Niranjan Khadka ran the model, collected data, and analyzed the data. Marom Bikson edited and revised the manuscript. Irene E. Harmen and Andres M Lozano provided important inputs and revised the manuscript. All authors approved the final manuscript.

## How to Cite this Article:

Khadka N., Harmsen I.E., Lozano A.M., Bikson M. 2020. Bio-Heat Model of Kilohertz-Frequency Deep Brain Stimulation Increases Brain Tissue Temperature. *Neuromodulation* 2020; E-pub ahead of print. DOI:10.1111/ner.13120

## REFERENCES

- Harmsen IE, Lee DJ, Dallapiazza RF et al. Ultra-high-frequency deep brain stimulation at 10,000 Hz improves motor function. *Mov Disord* 2019;34:146–148.
- Fagundes V de C, Rieder CRM, da Cruz AN, Beber BC, Portuguese MW. Deep brain stimulation frequency of the subthalamic nucleus affects phonemic and action fluency in Parkinson's disease. *Parkinsons Dis* 2016;2016:1–9.
- McIntyre CC, Chaturvedi A, Shamir RR, Lempka SF. Engineering the next generation of clinical deep brain stimulation technology. *Brain Stimul* 2015;8:21–26.
- Lozano AM, Lipsman N, Bergman H et al. Deep brain stimulation: current challenges and future directions. *Nat Rev Neurol* 2019;15:148–160.
- Benabid AL, Pollak P, Gervason C et al. Long-term suppression of tremor by chronic stimulation of the ventral intermediate thalamic nucleus. *Lancet* 1991; 337:403–406.
- Couto J, Grill WM. Kilohertz frequency deep brain stimulation is ineffective at regularizing the firing of model thalamic neurons. *Front Comput Neurosci* 2016; 10:1–12.
- Ramasubbu R, Lang S, Kiss ZHT. Dosing of electrical parameters in deep brain stimulation (DBS) for intractable depression: a review of clinical studies. *Front Psych* 2018;9:302.
- Cubo R, Fahlström M, Jiltsova E, Andersson H, Medvedev A. Calculating deep brain stimulation amplitudes and power consumption by constrained optimization. *J Neural Eng* 2019;16:016020.
- Kapur L, Yu C, Doust MW et al. Comparison of 10-kHz high-frequency and traditional low-frequency spinal cord stimulation for the treatment of chronic back and leg pain: 24-month results from a Multicenter, randomized, controlled pivotal trial. *Neurosurgery* 2016;79:667–677.
- Crosby ND, Janik JJ, Grill WM. Modulation of activity and conduction in single dorsal column axons by kilohertz-frequency spinal cord stimulation. *J Neurophysiol* 2017;117:136–147.
- Al-Kaisy A, Van Buyten J-P, Smet I, Palmisani S, Pang D, Smith T. Sustained effectiveness of 10 kHz high-frequency spinal cord stimulation for patients with chronic, low back pain: 24-month results of a prospective multicenter study. *Pain Med* 2014;15:347–354.
- Shechter R, Yang F, Xu Q et al. Conventional and kilohertz-frequency spinal cord stimulation produces intensity- and frequency-dependent inhibition of mechanical hypersensitivity in a rat model of neuropathic pain. *Anesthes* 2013;119: 422–432.
- Song Z, Viisanen H, Meyerson BA, Pertovaara A, Linderth B. Efficacy of kilohertz-frequency and conventional spinal cord stimulation in rat models of different pain conditions. *Neuromodulation* 2014;17:226–235.
- Zannou AL, Khadka N, Truong DQ et al. Temperature increases by kilohertz frequency spinal cord stimulation. *Brain Stimul* 2019;12:62–72.
- Elwassif MM, Kong Q, Vazquez M, Bikson M. Bio-heat transfer model of deep brain stimulation-induced temperature changes. *J Neural Eng* 2006;3:306–315.
- Elwassif MM, Datta A, Rahman A, Bikson M. Temperature control at DBS electrodes using a heat sink: experimentally validated FEM model of DBS lead architecture. *J Neural Eng* 2012;9:046009.
- Grill WM, Mortimer JT. Electrical properties of implant encapsulation tissue. *Ann Biomed Eng* 1994;22:23–33.
- Collins CM, Smith MB, Turner R. Model of local temperature changes in brain upon functional activation. *J Appl Physiol* 2004;97:2051–2055.
- Xu X, Tikuisis P, Giesbrecht G. A mathematical model for human brain cooling during cold-water near-drowning. *J Appl Physiol* 1999;86:265–272.
- Hodson DA, Barbenel JC, Eason G. Modelling transient heat transfer through the skin and a contact material. *Phys Med Biol* 1989;34:1493–1507.
- Wilson SB, Spence VA. A tissue heat transfer model for relating dynamic skin temperature changes to physiological parameters. *Phys Med Biol* 1988;33: 895–912.
- Fiala D, Lomas KJ, Stohrer M. A computer model of human thermoregulation for a wide range of environmental conditions: The passive system. *J Appl Physiol* 1999;87:1957–1972.
- Gabriel S, Lau RW, Gabriel C. The dielectric properties of biological tissues: III. Parametric models for the dielectric spectrum of tissues. *Phys Med Biol* 1996;41: 2271–2293.

24. Hasgall PA, Di Gennaro F, Baumgartner C et al. IT'IS Database for thermal and electromagnetic parameters of biological tissues, Version 4.0, May 15, 2018, itis.swiss/database
25. Butson CR, McIntyre CC. Role of electrode design on the volume of tissue activated during deep brain stimulation. *J Neural Eng* 2006;3:1–8.
26. Zannou AL, Khadka N, FallahRad M, Truong DQ, Kopell BH, Bikson M. Tissue temperature increases by a kHz spinal cord stimulation system: phantom and bioheat model. *Neuromodulation* 2019. <https://doi.org/10.1111/ner.12980>
27. Khadka N, Bikson M. Response to the letter to the editor by caraway et al. on "tissue temperature increases by a 10 kHz spinal cord stimulation system: phantom and bioheat model." *Neuromodulation* 2019;22:988–988.
28. Elwassif MM, Kong Q, Vazquez M, Bikson M. *Bio-heat transfer model of deep brain stimulation induced temperature changes*. In: 28th Annual International Conference of the IEEE Engineering in Medicine and Biology Society, 2006. EMBS'06, 2006:3580–3583.
29. Rattay F. Analysis of models for external stimulation of axons. *IEEE Trans Biomed Eng* 1986;33:974–977.
30. Butson CR, McIntyre CC. Role of electrode design on the volume of tissue activated during deep brain stimulation. *J Neural Eng* 2005;3:1–8.
31. Chaturvedi A, Butson CR, Lempka SF, Cooper SE, McIntyre CC. Patient-specific models of deep brain stimulation: influence of field model complexity on neural activation predictions. *Brain Stimul* 2010;3:65–67.
32. Astrom M, Diczfalusy E, Martens H, Wardell K. Relationship between neural activation and electric field distribution during deep brain stimulation. *IEEE Trans Biomed Eng* 2015;62:664–672.
33. Hemm S, Mennessier G, Vayssière N, Cif L, Coubes P. Co-registration of stereotactic MRI and isofieldlines during deep brain stimulation. *Brain Res Bull* 2005;68:59–61.
34. Horn A, Reich M, Vorwerk J et al. Connectivity predicts deep brain stimulation outcome in Parkinson disease. *Ann Neurol* 2017;82:67–78.
35. Philpott JM, Zemlin CW, Damiano R. Chapter 4 - the art and science of making effective maze ablation lines. In: Philpott JM, Zemlin CW, Damiano R, editors. *Surgical treatment of atrial fibrillation*. Cambridge, MA: Academic Press, 2017; p. 63–96.
36. Health C for D and R. Assessment of radiofrequency-induced heating in the magnetic resonance (MR) environment for multi-configuration passive medical devices. US Food and Drug Administration, 2019.
37. Kainz W, Neubauer G, Überbacher R, Alesch F, Chan DD. Temperature measurement on neurological pulse generators during MR scans. *Biomed Eng Online* 2002;1:2.
38. Golestanirad L, Kirsch J, Bonmassar G et al. RF-induced heating in tissue near bilateral DBS implants during MRI at 1.5 T and 3T: The role of surgical lead management. *Neuroimage* 2019;184:566–576.
39. Brodkey JS, Miyazaki Y, Ervin FR, Mark VH. Reversible heat lesions with radio-frequency current: a method of stereotactic localization. *J Neurosurg* 1964;21:49–53.
40. Eve FC. The effect of temperature on the functional activity of the upper cervical ganglion. *J Physiol* 1900;26:119–124.
41. Butson CR, Cooper SE, Henderson JM, McIntyre CC. Patient-specific analysis of the volume of tissue activated during deep brain stimulation. *Neuroimage* 2007;34:661–670.
42. Walckiers G, Fuchs B, Thiran J-P, Mosig JR, Pollo C. Influence of the implanted pulse generator as reference electrode in finite element model of monopolar deep brain stimulation. *J Neurosci Methods* 2010;186:90–96.
43. Grant PF, Lowery MM. Electric field distribution in a finite-volume head model of deep brain stimulation. *Med Eng Phys* 2009;31:1095–1103.
44. Butson CR, Moks CB, McIntyre CC. Sources and effects of electrode impedance during deep brain stimulation. *Clin Neurophysiol* 2006;117:447–454.
45. McIntyre CC, Savasta M, Kerkerian-Le Goff L, Vitek JL. Uncovering the mechanism(s) of action of deep brain stimulation: activation, inhibition, or both. *Clin Neurophysiol* 2004;115:1239–1248.
46. McIntyre CC, Thakor NV. Uncovering the mechanisms of deep brain stimulation for Parkinson's disease through functional imaging, neural recording, and neural modeling. *Crit Rev Biomed Eng* 2002;30:249–281.
47. McIntyre CC, Savasta M, Walter BL, Vitek JL. How does deep brain stimulation work? Present understanding and future questions. *J Clin Neurophysiol* 2004;21:40–50.
48. Frankemolle AMM, Wu J, Noecker AM et al. Reversing cognitive-motor impairments in Parkinson's disease patients using a computational modelling approach to deep brain stimulation programming. *Brain* 2010;133:746–761.
49. Kim JA, Connors BW. High temperatures alter physiological properties of pyramidal cells and inhibitory interneurons in hippocampus. *Front Cell Neurosci* 2012;6:27.
50. Harris AB, Erickson L, Kendig JH, Mingrino S, Goldring S. Observations on selective brain heating in dogs. *J Neurosurg* 1962;19:514–521.
51. Matsumi N, Matsumoto K, Mishima N et al. Thermal damage threshold of brain tissue—histological study of heated normal monkey brains. *Neurol Med Chir (Tokyo)* 1994;34:209–215.
52. Chowdhury S, Jarecki BW, Chanda B. A molecular framework for temperature-dependent gating of ion channels. *Cell* 2014;158:1148–1158.
53. Graham BA, Brichta AM, Callister RJ. Recording temperature affects the excitability of mouse superficial dorsal horn neurons, in vitro. *J Neurophysiol* 2008;99:2048–2059.
54. Darrow DP, O'Brien P, Richner TJ, Netoff TI, Ebbini ES. Reversible neuroinhibition by focused ultrasound is mediated by a thermal mechanism. *Brain Stimul* 2019;12:1439–1447.
55. Duke AR, Jenkins MW, Lu H, McManus JM, Chiel HJ, Jansen ED. Transient and selective suppression of neural activity with infrared light. *Sci Rep* 2013;3:1–8.
56. Cubo R, Medvedev A, Åström M. Model-based optimization of individualized deep brain stimulation therapy. *IEEE Des Test* 2016;33:74–81.
57. Alonso F, Latorre MA, Göransson N, Zsigmond P, Wårdell K. Investigation into deep brain stimulation Lead designs: a patient-specific simulation study. *Brain Sci* 2016;6:39.
58. Lempka SF, Johnson MD, Miocinovic S, Vitek JL, McIntyre CC. Current-controlled deep brain stimulation reduces in vivo voltage fluctuations observed during voltage-controlled stimulation. *Clin Neurophysiol* 2010;121:2128–2133.
59. Cubo R, Åström M, Medvedev A. Optimization of lead design and electrode configuration in deep brain stimulation. *Int J Adv Life Sci* 2016;8:76–86.
60. Anderson DN, Osting B, Vorwerk J, Dorval AD, Butson CR. Optimized programming algorithm for cylindrical and directional deep brain stimulation electrodes. *J Neural Eng* 2018;15:026005.
61. Dembek TA, Reker P, Visser-Vandewalle V et al. Directional DBS increases side-effect thresholds—a prospective, double-blind trial. *Mov Disord* 2017;32:1380–1388.
62. Pollo C, Kaelin-Lang A, Oertel MF et al. Directional deep brain stimulation: An intraoperative double-blind pilot study. *Brain* 2014;137:2015–2026.
63. Foutz T, McIntyre C. Evaluation of novel stimulus waveforms for deep brain stimulation. *J Neural Eng* 2010;7:066008.
64. Wei XF, Grill WM. Impedance characteristics of deep brain stimulation electrodes in vitro and in vivo. *J Neural Eng* 2009;6:046008.
65. Oza CS, Brocker DT, Behrend CE, Grill WM. Patterned low-frequency deep brain stimulation induces motor deficits and modulates cortex-basal ganglia neural activity in healthy rats. *J Neurophysiol* 2018;120:2410–2422.
66. Grill WM. Temporal pattern of electrical stimulation is a new dimension of therapeutic innovation. *Curr Opin Biomed Eng* 2018;8:1–6.
67. Kim D, Jeong J, Jeong S, Kim S, Jun SC, Chung E. Validation of computational studies for electrical brain stimulation with phantom head experiments. *Brain Stimul* 2015;8:914–925.
68. Howell B, Choi KS, Gunalan K, Rajendra J, Mayberg HS, McIntyre CC. Quantifying the axonal pathways directly stimulated in therapeutic subcallosal cingulate deep brain stimulation. *Hum Brain Mapp* 2019;40:889–903.
69. Ramirez-Zamora A, Giordano J, Boyden ES et al. Proceedings of the sixth deep brain stimulation think tank modulation of brain networks and application of advanced neuroimaging, neurophysiology, and Optogenetics. *Front Neurosci* 2019;13:936.
70. Lopez-Quintero SV, Datta A, Amaya R, Elwassif M, Bikson M, Tarbell JM. DBS-relevant electric fields increase hydraulic conductivity of in vitro endothelial monolayers. *J Neural Eng* 2010;7:16005.

## COMMENT

Khadka and colleagues present an important and novel computational model of the potential therapeutic impact of thermal changes related to 10 KHz deep brain stimulation. While clinical correlation will be critical, the importance of this manuscript lies in opening the eyes of the neuromodulation community to novel mechanisms of modulation, beyond electrochemical effects of stimulation. We have long known that tissue heating affects function and in the era of non-lesional neuromodulation. As a result, we have been vigilant about controlling for such temperature changes to minimize the potential chronic, irreversible "injury." With the computational modeling presented here, we must begin to think about the potential therapeutic role of low level temperature changes that may be reversible and beneficial. While still not clinically proven, we should keep our eyes open to the potential value of such an approach.

Nader Pouratian, MD  
Los Angeles, CA, USA